Boundary-Layer Meteorology (2005) 115: 289–317

THE SUMMER SURFACE ENERGY BALANCE OF THE HIGH ANTARCTIC PLATEAU

DIRK VAN AS*, MICHIEL VAN DEN BROEKE, CARLEEN REIJMER and RODERIK VAN DE WAL

Institute for Marine and Atmospheric Research Utrecht (IMAU), Utrecht University, P.O. Box 80000, 3508 TA Utrecht, The Netherlands

(Received in final form 16 September 2004)

Abstract. The summertime surface energy balance (SEB) at Kohnen station, situated on the high Antarctic plateau (75°00′ S, 0°04′ E, 2892 m above sea level) is presented for the period of 8 January to 9 February 2002. Shortwave and longwave radiation fluxes were measured directly; the former was corrected for problems associated with the cosine response of the instrument. Sensible and latent heat fluxes were calculated using the bulk method, and eddy-correlation measurements and the modified Bowen ratio method were used to verify these calculated fluxes. The calculated sub-surface heat flux was checked by comparing calculated to measured snow temperatures. Uncertainties in the measurements and energy-balance calculations are discussed.

The general meteorological conditions were not extraordinary during the period of the experiment, with a mean 2-m air temperature of −27.5 °C, specific humidity of 0.52×10^{-3} kg kg^{-1} and wind speed of 4.1 m s^{-1}. The experiment covered the transition period from Antarctic summer (positive net radiation) to winter (negative net radiation), and as a result the period mean net radiation, sensible heat, latent heat and sub-surface heat fluxes were small with values of −1.1, 0.0, −1.0 and 0.7 W m^{-2}, respectively. Daily mean net radiation peaked on cloudy days (16 W m^{-2}) and was negative on clear-sky days (minimum of −19 W m^{-2}). Daily mean sensible heat flux ranged from −8 to +10 W m^{-2}, latent heat flux from −4 to 0 W m^{-2} and sub-surface heat flux from −8 to +7 W m^{-2}.

Keywords: Antarctica, Atmospheric surface layer, Boundary-layer experiment, ENABLE, Snow, Turbulent heat fluxes.

1. Introduction

Energy exchange at the Earth's surface is governed by the surface energy balance (SEB); for a non-melting snow surface this energy balance can be written as:

$$S_{\downarrow} + S_{\uparrow} + L_{\downarrow} + L_{\uparrow} + H + \lambda_s E + G = 0, \quad (1)$$

where S and L denote the incoming and outgoing shortwave and longwave radiation fluxes, respectively, H is the sensible heat flux, $\lambda_s E$ the latent heat flux and G the sub-surface heat flux. All components are defined positive towards the surface.

* E-mail: D.vanAs@phys.uu.nl

The SEB of Antarctica is extreme. Most of the Antarctic ice sheet is characterised by a high surface albedo, reflecting 80–90% of the solar radiation and leaving little energy to heat the surface in summer. During daytime weak convection is capable of creating a thin, unstably stratified atmospheric boundary layer. At night and during the winter the snow surface is generally cooled by a negative net longwave radiation (L_N), which is enabled by clear-sky conditions and the very cold and dry overlying atmosphere. Since the sensible heat flux acts to decrease the temperature difference between the surface and the atmospheric surface layer, the latter cools as well and thus becomes denser than the free atmosphere aloft. In this negatively buoyant state, the surface layer flows down the slope of the ice sheet, deflected to the left by the Coriolis force. These are the well-known katabatic winds, and, in turn, the katabatic winds interact strongly with the surface energy fluxes as turbulent heat transport increases with wind speed under stable stratification. These strong winds interact with the surface mass balance through enhanced sublimation and snowdrift, which is best seen in blue ice areas, emphasising the importance of the SEB for the meteorology and mass balance of Antarctica.

Several observational studies have addressed the SEB in Antarctica, e.g., Wendler et al. (1988), King and Anderson (1994), Bintanja and Van den Broeke (1995), King et al. (1996), Reijmer et al. (1999) and Bintanja (2000). Most observations are confined to the coastal regions of the continent (e.g. König-Langlo et al., 1998) and to the summer period. The interior has a relatively poor spatial observational coverage (Dalrymple et al., 1966; Weller, 1980; Carroll, 1982; King and Turner, 1997), limited to the surroundings of inland bases.

To be able to determine the SEB of remote areas, automatic weather stations (AWSs) offer a solution. The low energy consumption of an AWS allows placement far away from manned stations and reduces the need for frequent visits, enabling year-round measurements of surface-layer meteorology. Records of AWSs around Antarctica have been presented by e.g., Allison et al. (1993), Stearns and Weidner (1993), Jonsson (1995) and Reijmer and Oerlemans (2002). However, AWS observations are often limited to one vertical level in the atmospheric surface layer, and sensor failure may result in data gaps.

Alternatively, the SEB of Antarctica can be studied using atmospheric models. Model simulations provide a useful tool to fill the gaps in space and time, so to better comprehend spatial and temporal variability of the SEB. Numerical models have clear advantages over measurement campaigns, since they are not confined to one location or time of year, but describe the three-dimensional structure of the atmosphere at high resolution and over vast areas. Model simulation is a cheap alternative to the high-cost logistics associated with polar expeditions and has provided valuable results (Fortuin

and Oerlemans, 1992; Genthon and Braun, 1995; King and Connolley, 1997; Van den Broeke et al., 1997; Van Lipzig et al., 1999), for example by showing that there is a large variability in turbulent heat fluxes across the continent. Nevertheless, it is essential that numerical models are validated by observations.

The EPICA-Netherlands Atmospheric Boundary Layer Experiment (ENABLE) was performed at Kohnen station (75°00′ S, 0°04′ E, 2892 m above sea level) in Dronning Maud Land (DML), East Antarctica (Figure 1), from 8 January to 9 February 2002. The campaign set out to obtain atmospheric profiles of wind speed and direction, temperature and humidity covering the lowest 20 km of the atmosphere by profile masts, tethered balloon and radiosondes. In addition, detailed and high-frequency measurements of the radiation budget, turbulent heat fluxes through eddy-correlation measurements, sub-surface temperatures and snowdrift measurements were performed. Kohnen base is one of the two drilling locations of EPICA (European Project for Ice Coring in Antarctica). Three years prior to the start of the drilling operation, in January 1998, an AWS

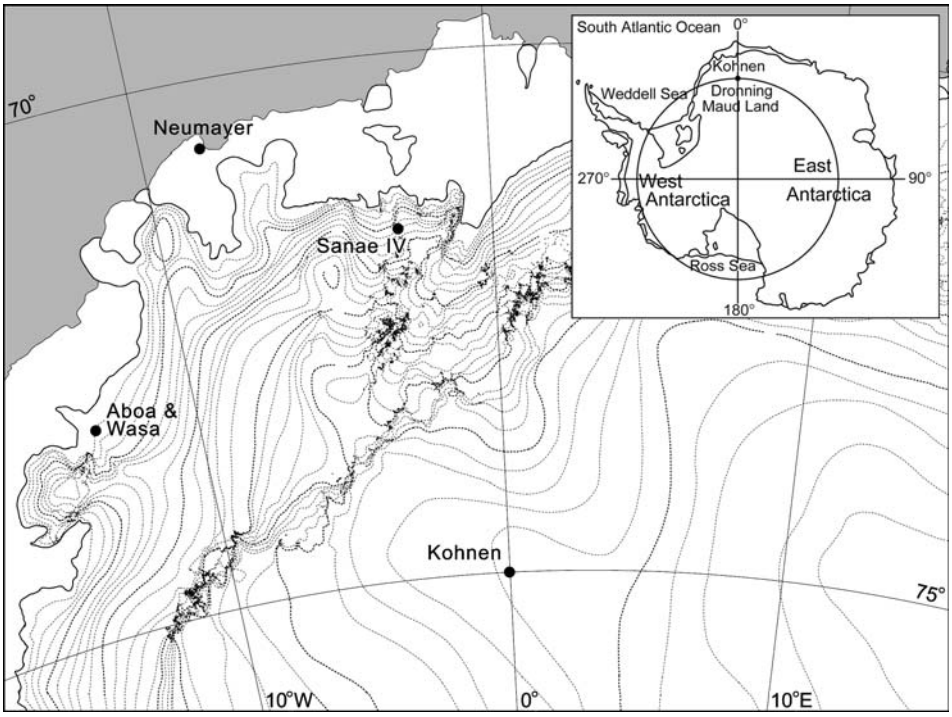

Figure 1. Map of Dronning Maud Land (DML) with the location of Kohnen station (75°00′S, 0°04′E, 2892 m altitude). Contour lines are drawn for every 100 m of surface elevation.

was installed (AWS 9) at 1.8 km from the future location of ENABLE. ENABLE also serves to supplement the meteorological observations collected by this AWS.

This paper presents the summer SEB at Kohnen station as determined from measurements during ENABLE. In Section 2 we describe the instrumentation and data treatment. Since direct measurements of G and $\lambda_s E$ were not performed and eddy-correlation measurements of H do not cover the entire period, these components of the SEB were calculated using techniques discussed in Section 3. The measurements and SEB are then presented in Section 4, whereafter in Section 5 a discussion follows and conclusions are drawn.

2. Instrumentation and Data Treatment

2.1. Sensor description

In Antarctica much is demanded from the equipment used in meteorological experiments, as most sensors are not designed to operate at low temperatures. Sensor sensitivity is of importance as well; compared to a mid-latitude location parameters such as specific humidity (q) show small absolute variability, which means that errors of measurement can have a relatively large impact.

Details of the various sensors used during ENABLE are given in Table I. We use down-welling and upwelling broadband shortwave and longwave radiation as measured once a minute by a Kipp & Zonen CNR1 combined pyranometer and pyrradiometer. These sensors were tested after the experiment by placing them nearby ($\approx$ 200 m) the Neumayer (70°39′ S, 08°15′ W, Figure 1) radiation sensors for the period from 18 to 27 February 2002. Neumayer radiation measurements are performed within the Baseline Surface Radiation Network, and therefore have a high absolute accuracy. $S_\downarrow$ has a RMSD (root mean square difference) of 9 W m^{-2} for 2-h means. For daily totals the RMSD is $\approx$ 2.7%, which is much better than the factory specifications in Table I. $L_\downarrow$ is also in good agreement with the Neumayer data and has a RMSD of 3.3 W m^{-2} ($\approx$1.2% for daily totals), though a mean difference of 2.6 W m^{-2} does signify a small systematic bias. A more detailed discussion of measurement errors of radiation is given by Van den Broeke et al. (2004b). In the next section we briefly repeat their method to improve the quality of shortwave data. Radiation sensors of a higher standard that were also deployed during ENABLE (Kipp & Zonen CM14 for shortwave radiation and Eppley PIR for longwave radiation) were found to have more problems with icing and are therefore not used here.

TABLE I
Sensor specifications: instrument type, parameter measured, resolution, estimated accuracy and temperature calibration range. FDT: for daily totals.

Sensor	Parameter(s)	Resolution	Accuracy	Calibration range
Kipp & Zonen	$S\downarrow$, $S\uparrow$		10% FDT	−40 to +70 °C
CNR1	$L\downarrow$, $L\uparrow$		10% FDT	
Vaisala HMP35C	T		0.2 °C	−55[a] to +60 °C
Temperature and	RH		2% (RH < 90%)	
relative humidity			3% (RH > 90%)	
probe (ventilated)				
Vector A100R cup	u		0.1 m s^{-1}	
anemometer				
Campbell CSAT3	u', v′	1 mm s^{-1}		−38[a] to +50 °C
3D Sonic	w'	0.5 mm s^{-1}		
anemometer	T'	2×10^{-3} °C		
107 Thermistor	T_{snow}		<0.5 °C	−80[a] to +50 °C
temperature probe				

[a]Sensors or calibration polynomials were modified for low temperature performance.

Temperature (T) and relative humidity (RH) were sampled every 2 min at five heights (0.5, 1, 2, 5 and 10 m) with ventilated Vaisala HMP35C probes; cup anemometers were installed at the same heights to measure wind speed (u). Sub-surface temperature was measured at five depths (0.05, 0.1, 0.2, 0.3 and 0.4 m).

Furthermore, direct turbulent flux measurements were carried out using fast-response anemometers. Two Campbell CSAT3 sonic anemometers measured the three orthogonal components of the wind and the temperature at 20 Hz (installed at 2 and 10 m), while a third and identical anemometer was placed at 2-m height, sampling at a frequency of 1 Hz, and programmed to store 10-min averages of all parameter covariances. The fast and slow sampling set-ups produced very similar results. Data spikes were removed by applying threshold values. Mild threshold values were chosen to avoid removal of spikes caused by turbulent bursting in the stable boundary layer. Sonic anemometer measurements were corrected for tilt by applying the planar fit method (Wilczak et al., 2001). Side-wind correction of temperature is performed internally by the Campbell CSAT3. No direct measurements of $\lambda_s E$ are available in this study, complicating humidity flux correction of sonic heat flux measurements (Schotanus et al., 1983). Using a calculated latent heat flux indicates that this brings about an approximate 2% error of the sonic heat flux in unstable stratification and a 0.5% error in stable

stratification. The error is small, owing to the low water content of the cold Antarctic boundary layer.

Most sensors functioned continuously during the period described herein. However, sub-surface temperatures are only available during the final 13 days of the experiment due to a data logger problem. No eddy-correlation data were stored below approximately −38 °C, resulting in several nighttime data gaps.

2.2. Data treatment

2.2.1. *Net Shortwave Radiation*

Net shortwave radiation (S_N) is the most important source of energy for the surface during the short Antarctic summer. Calculations of S_N from raw $S_\downarrow$ and $S_\uparrow$ data can be inaccurate for several reasons, such as a tilted sensor or icing. During ENABLE, tilt was checked daily and estimated to be smaller than 0.5°; icing occurred infrequently. More importantly, shortwave radiation sensors sometimes have difficulties in accurately measuring solar radiation originating from large zenith angles (a poor cosine response). For the reflected component, as well as for $S_\downarrow$ during overcast conditions, this problem does not occur since the shortwave radiation will be largely diffuse and only a small part of the irradiance will originate from large zenith angles. During clear-sky conditions, however, low solar elevation causes a serious problem. According to the CNR1 sensor manual, measurements of $S_\downarrow$ 'yield unreliable results' for zenith angles larger than approximately 80°. Since the experiment was performed at the end of the Antarctic summer solar zenith angles were generally large. Zenith angles larger than 80° occurred during approximately 30% of the experiment. The measured instantaneous albedo ($\alpha = |S_\uparrow|/S_\downarrow$) was occasionally unrealistically high during the night, exceeding unity, causing an underestimate of net shortwave radiation by up to 20 W m^{-2}. As this degree of inaccuracy is unacceptable, a method was devised to overcome this problem.

The incoming shortwave radiation accumulated over a day is hardly affected by a poor cosine response, as the major contribution (approximately 93%) arises from periods when the solar zenith angle is smaller then 80°. Therefore, we use the accumulated albedo, which removes the effects associated with the poor cosine response from S_N (Van den Broeke et al., 2004b):

$$\alpha_{ac} = -\frac{\sum_{24\,h} S_\uparrow}{\sum_{24\,h} S_\downarrow}, \tag{2}$$

where data of the 12 h preceding and following the time of observation are used. Then α_{ac} can be used to calculate the instantaneous net shortwave radiation using:

$$S_N = S_\downarrow + S_\uparrow = \frac{-S_\uparrow}{\alpha_{ac}} + S_\uparrow = S_\uparrow\left(1 - \frac{1}{\alpha_{ac}}\right), \quad (3)$$

thus using $S_\uparrow$ measurements, which are unaffected by a poor cosine response, as a basis for the calculation of $S_\downarrow$.

However, this method removes the daily variation of the albedo caused by changes in solar zenith angle (i.e. the change of the diffuse fraction of the sunlight (δ)). Therefore, an artificial daily cycle in broadband albedo is derived from the analytical model of Wiscombe and Warren (1980), who proposed that the albedo of snow depends on snow grain size and δ. Here, we assume that the snow grain size has a constant value of 10^{-4} m. The diffuse fraction of $S_\downarrow$ is a function of cloud cover and path length through the atmosphere. The path length is determined using the solar zenith angle; cloud cover can be estimated from $L_\downarrow$ and temperature due to the emissive properties of clouds and its effect on near-surface temperature. The latter is visualised in a scatter plot of $L_\downarrow$ versus 2-m temperature (Figure 2) measured by the nearby AWS 9 over a four-year period. For any temperature, the upper limit of $L_\downarrow$ is set under cloudy conditions and the lower limit under clear-sky conditions. Fitting temperature-dependent polynomials to the 5th and 95th percentiles of $L_\downarrow$ values gives the empirical relationships between $L_\downarrow$ and 2-m temperature for cloudy and clear skies (respectively $L_{\downarrow,\mathrm{clear}}(T)$ and

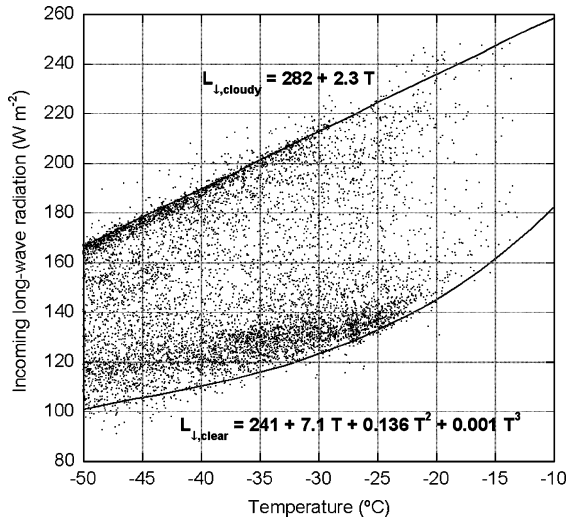

Figure 2. The dependence of 2-m temperature on $L_\downarrow$ at Kohnen station based on four years of 2-h mean AWS data. The upper line shows the approximate relationship between the two parameters for overcast conditions, the lower line for clear sky conditions.

$L_{\downarrow,\mathrm{cloudy}}(T)$). The diffuse fraction of $S_{\downarrow}$ at any time is then estimated by linear interpolation between these polynomials:

$$\delta(L_{\downarrow}, T) = \delta_{\min} + (1 - \delta_{\min}) \frac{\left(L_{\downarrow} - L_{\downarrow,\mathrm{clear}}(T)\right)}{\left(L_{\downarrow,\mathrm{cloudy}}(T) - L_{\downarrow,\mathrm{clear}}(T)\right)}, \tag{4}$$

where $\delta_{\min}$ is the δ under clear-sky conditions, and is set to 0.2. The diffuse fraction derived from this equation is used in the theoretical albedo calculation. Hereafter, the artificial daily cycle in albedo is added to α_{ac} in such a fashion that S_{N} accumulated over a day remains unchanged.

2.2.2. *Relative Humidity*

The Vaisala HMP35C relative humidity probe measures relative humidity with respect to water instead of ice. At sub-zero temperatures this causes the relative humidity readings to be unrealistically low. Moreover, the HMP35C has an off-factory calibration down to −20 °C, below which the measured RH exhibits an unrealistic cut-off at values well below 100%. Anderson (1994) proposes a two-step method to re-scale the measured relative humidity to obtain more accurate values. This method was applied successfully to Greenland and Antarctic AWS data (Box and Steffen, 2001; Van den Broeke et al., 2004a, respectively) and also used to correct the ENABLE RH data. Relative humidity was converted to specific humidity using the saturation vapour pressure relation of Curry and Webster (1999).

3. Energy Balance Calculations

The SEB calculations consist of an atmospheric and a sub-surface part. The atmospheric part calculates the turbulent heat fluxes using the bulk method; the sub-surface part calculates heat transport in the snow.

3.1. Turbulent heat fluxes

In accordance with Monin–Obukhov similarity theory, the sensible and latent heat fluxes can be expressed as

$$H = \rho c_{\mathrm{p}} u_* T_*, \tag{5}$$

$$\lambda_{\mathrm{s}} E = \rho \lambda_{\mathrm{s}} u_* q_*, \tag{6}$$

where ρ denotes air density, $c_{\mathrm{p}} = 1005$ J K^{-1} kg^{-1} is the specific heat of dry air at constant pressure, E is sublimation and $\lambda_s = 2.83 \times 10^6$ J kg^{-1} is the latent heat of sublimation. u_* is the friction velocity and T_* and q_* are the turbulent scales of temperature and humidity, defined as:

$$u_* = \left(\overline{u'w'}\right)^{0.5} \approx \frac{\kappa u(z)}{\ln\left(\frac{z}{z_0}\right) - \psi_{\mathrm{m}}(\xi)}, \tag{7}$$

$$T_* = \left(\overline{w'T'}\right)u_*^{-1} \approx \frac{\kappa(T(z) - T(0))}{\ln\left(\frac{z}{z_T}\right) - \psi_{\mathrm{h}}(\xi)}, \tag{8}$$

$$q_* = \left(\overline{w'q'}\right)u_*^{-1} \approx \frac{\kappa(q(z) - q(0))}{\ln\left(\frac{z}{z_q}\right) - \psi_{\mathrm{q}}(\xi)}, \tag{9}$$

where $\overline{u'w'}$, $\overline{w'T'}$ and $\overline{w'q'}$ are the surface kinematic fluxes of momentum, heat and moisture, respectively, u' and w' are the horizontal and vertical turbulent wind speed fluctuations, and q' is the fluctuation in specific humidity; $\kappa = 0.4$ is the Von Kármán constant. In the bulk approximation u, T and q at height z (≈ 2 m) and the surface roughness lengths associated with these parameters (z_0, z_T and z_q) determine the size of the associated turbulent scales. The surface roughness lengths are defined as the height where the downward extrapolated profiles of these parameters attain their surface values. The stability correction functions for momentum (ψ_{m}), heat (ψ_{h}) and humidity (ψ_{q}) depend solely on a non-dimensional stability parameter $\xi = z/L_*$,where L_* is the Obukhov length scale, defined as $L_* = u_*^2\theta_{\mathrm{v}}/g\kappa\theta_{\mathrm{v}*}$, where θ_{v} and $\theta_{\mathrm{v}*}$ are the virtual potential temperature and its turbulent scale. Here the functions determined by Holtslag and De Bruin (1988) were used for stable stratification, as recommended by Andreas (2002) after comparing several different stability correction functions, and those by Paulson (1970) and Dyer (1974) for unstable stratification (N.B.: Dyer used $\kappa = 0.41$). Turbulent Prandtl and Schmidt numbers are assumed equal to unity.

Even though wind speed, temperature and humidity were measured at more than one level and the two-level method often compares favourably with eddy-correlation measurements (Box and Steffen, 2001), the more robust one-level bulk method is chosen as the preferred method in this study. The two-level method is more sensitive to measurement errors given the small gradients higher above the surface. Using surface values instead of a second atmospheric measurement level increases the difference in T, q and u between the two levels, reducing the relative size of the measurement errors (see Figure 9 of Bintanja and Van den Broeke, 1995).

Some unknown parameters remain in Equations (5) through (9), namely the roughness lengths z_0, z_T and z_q, and the surface values of temperature $T(0)$ and specific humidity $q(0)$.

3.1.1. *Roughness Lengths*

During the experiment the visual roughness elements of the snow surface did not change significantly. Sastrugi (snow dunes) were present, which were small and had a low aspect ratio. The low temperatures prohibited fast snow crystal transformation. Therefore it was assumed that a constant value of z_0 could be used for the entire experiment. The value of z_0 is found to be 2×10^{-5} m as determined from eddy-correlation measurements, which is a very low value even for a snow surface (Bintanja and Van den Broeke, 1995).

Andreas (1987) suggests second-order polynomials to relate the roughness lengths for heat and moisture to z_0:

$$z_{T,q} = z_0 \exp\big(b_0 + b_1 \ln(\mathrm{Re}_*) + b_2 \ln^2(\mathrm{Re}_*)\big), \tag{10}$$

where Re_* is the roughness Reynolds number, defined as $\mathrm{Re}_* = u_* z_0 / v$. Here $v = 1.46 \times 10^{-5}$ m^2 s^{-1} is the kinematic viscosity of air. Andreas splits up the aerodynamic domain in three parts (smooth, transitional and rough) and defined different polynomial coefficients $b_{0,1,2}$ for each domain (Table II). Equation (10) is plotted in Figure 3 to give insight into the dependence of the roughness lengths on Re_*. The figure shows that both z_T and z_q are larger than z_0 for smooth flow, but decrease in size when the flow becomes more rough. During ENABLE Re_* did not exceed 0.7 (indicated by the grey area in the figure), which results in z_T and z_q being almost constant and larger than z_0. The validity of Equation (10) was discussed and confirmed by Andreas (2002), although some doubt remains about the validity of z_q due to a lack of measurements.

3.1.2. *Surface Temperature and Humidity*

Surface temperature is assumed equal to the radiative temperature determined from longwave radiation. Snow emits radiation following Boltzmann's law:

$$-L_\uparrow = (1 - \varepsilon) L_\downarrow + \varepsilon \sigma T(0)^4, \tag{11}$$

TABLE II

Values of the coefficients in Equation (10) for estimating the scalar roughness lengths in three aerodynamic regimes according to Andreas (1987).

	z_h			z_q		
	b_0	b_1	b_2	b_0	b_1	b_2
Smooth ($\mathrm{Re}_* \le 0.135$)	1.250	0	0	1.610	0	0
Transition ($0.135 < \mathrm{Re}_* < 2.5$)	0.149	−0.550	0	0.351	−0.628	0
Rough ($\mathrm{Re}_* \ge 2.5$)	0.317	−0.565	−0.183	0.396	−0.512	−0.180

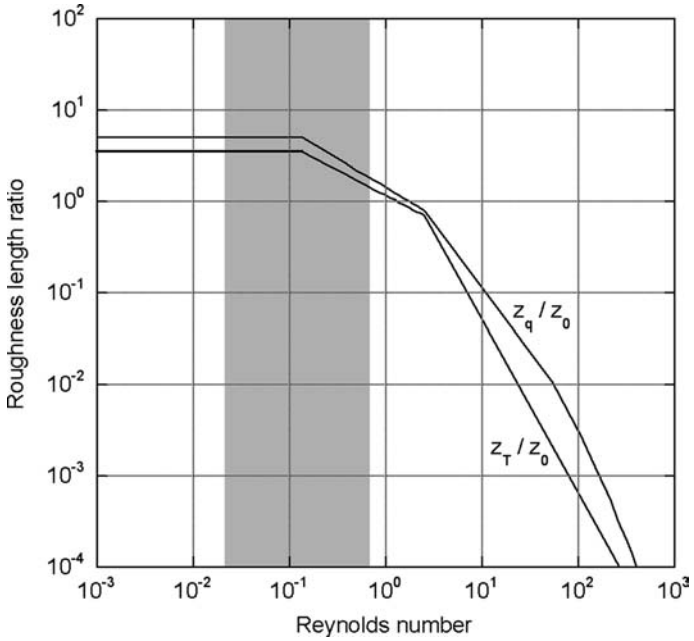

Figure 3. The ratio of z_T and z_q to z_0 plotted against the roughness Reynolds number, according to *Andreas* (1987). The grey area indicates the typical range of Re_* for ENABLE.

where $\sigma = 5.67 \times 10^{-8}$ W K^{-4} m^{-2} is the Stefan-Boltzmann constant, and ε is the broadband emissivity of the snow surface in the longwave part of the spectrum with a value close to unity. Due to the uncertainty of its value, here ε is set to 1. Surface humidity $q(0)$ is calculated from $T(0)$ under the assumption that the snow surface is continuously saturated with respect to ice.

In Section 2.1 we showed that the RMSD between CNR1 and Neumayer readings of longwave flux was 3.3 W m^{-2} for two-hourly means, with a systematic bias of 2.6 W m^{-2}. At the mean temperature during ENABLE this systematic bias is equivalent to an underestimation in surface temperature of about 0.8 °C. The random error on top of this bias is 2.2 W m^{-2}, which translates to a random error in half-hourly radiative temperature values of 1.3 °C. An uncertainty of approximately -0.8 ± 1.3 °C is acceptable for SEB calculations.

A second check of the accuracy of $T(0)$ obtained from $L\uparrow$ was performed by linearly extrapolating 50 and 100 mm snow temperatures to the surface ($T(0)_{extr}$) over all available measurements and comparing these with measured surface temperatures. From this we find that $T(0)-T(0)_{extr} \approx -0.9 \pm 1.3$ °C, which also indicates that no large systematic bias is present in the radiative surface temperature measurement. The effect of a systematic error of 1 °C is discussed in Section 4.3.

3.2. Sub-surface heat flux

Direct measurement of the sub-surface heat flux in snow is difficult because heat flux plates directly influence the structure and metamorphosis grade of the snow. Therefore a modelling approach to determine the sub-surface heat flow is preferable.

Neglecting shortwave radiation penetration into snow (which is justified according to Brandt and Warren, 1993) and wind ventilation of the upper snow layer, the thermodynamic equation of heat transport in snow simplifies considerably. Under the assumption of horizontal homogeneity the sub-surface heat flux follows from:

$$G = k_e(0)\left(\frac{\partial T}{\partial z}\right)_{z=0}, \tag{12}$$

where z is defined positive downwards.

Sub-surface heat flux calculations for ENABLE were initialised by a temperature profile that was determined from thermistor string measurements at AWS 9. The temperature profiles in all subsequent time steps were calculated using $T = T(0)$, determined from longwave flux measurements, and $(\partial T/\partial z)_{z\to\infty} = 0$ as upper and lower boundary conditions, respectively. The temperature gradient at the surface (needed in Equation (12)) then follows from the temperature difference between the surface and the first modelled snow layer, which was at 0.04 m depth in our calculations. k_e is an 'effective' conductivity parameter, since it embodies more than one process of heat transport. Conduction in the ice lattice, diffusive transport in air between snow grains and the sub-surface equivalents of the sensible and latent heat flux are all included in k_e. We used the empirical relationship for k_e produced by Östin and Andersson (1991), assuming dependence only on snow density:

$$k_e(z) = -0.00871 + 0.439 \times 10^{-3}\rho_s(z) + 1.05 \times 10^{-6}\rho_s(z)^2, \tag{13}$$

where ρ_s is snow density in kg m^{-3}. The density profile is obtained from six snow pits that were dug within a radius of 2 km of the Kohnen base. Figure 4 shows the mean snow density at depths up to 1.2 m, including standard deviation. Standard deviation increases with depth, due to a decreasing number of measurements. We applied a linear fit to these measurements to represent the density of the upper snow layer at Kohnen. Below 1.2 m depth the linear relationship is not accurate, but the temperature perturbations that occur at this depth during the ENABLE period are very small and have no influence on G at the surface. Figure 4 suggests a surface snow density of 323 kg m^{-3}, which, according to Equation (13), results in $k_e(0) = 24.3 \times 10^{-2}$ W K^{-1} m^{-1}.

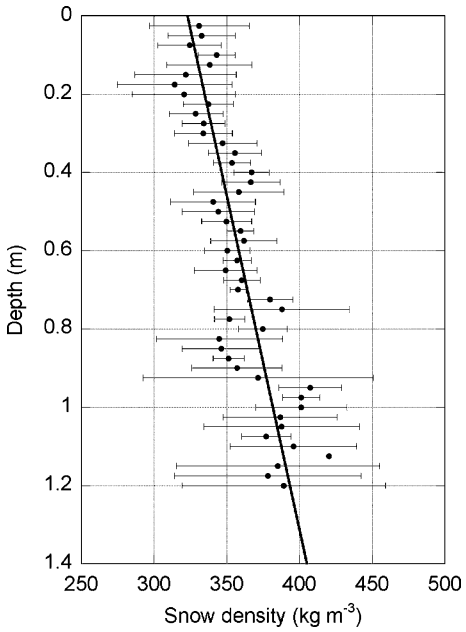

Figure 4. Mean snow density (dots) and standard deviation from measurements obtained from six snow pits in the vicinity of Kohnen station. The line indicates the best linear fit to the dots.

4. Results

4.1. General meteorological conditions

Kohnen station is positioned approximately 500 km from the coast on the high Antarctic plateau. Due to the location of the circumpolar pressure trough north of Antarctica, the mean synoptic pressure gradient forces an easterly geostrophic wind. Also the near-surface air flow is persistently westward; the directional constancy, defined as the ratio of the vector mean wind to the scalar mean wind speed, is 0.88 at AWS 9 (Reijmer, 2001). This high value indicates that it is likely that the near-surface flow has a katabatic component, forced by a slightly sloping surface of 1.3 ± 0.3 m km^{-1} in the east/north-easterly direction (61°, derived from the 1×1 km^2 Radarsat Antarctic Mapping Project Digital Elevation Model version 2 (Liu et al., 2001)).

Figure 5 shows daily averages of 2-m temperature, specific humidity and wind speed at AWS 9 for the 4-year period preceding the experiment. Annual averages for T, q and u are −43.2 °C, 0.17×10^{-3} kg kg^{-1} and 4.3 m s^{-1}, respectively. Temperature shows a strong seasonal cycle, ranging from a maximum of −15 °C in the short summer to almost −70 °C during the long

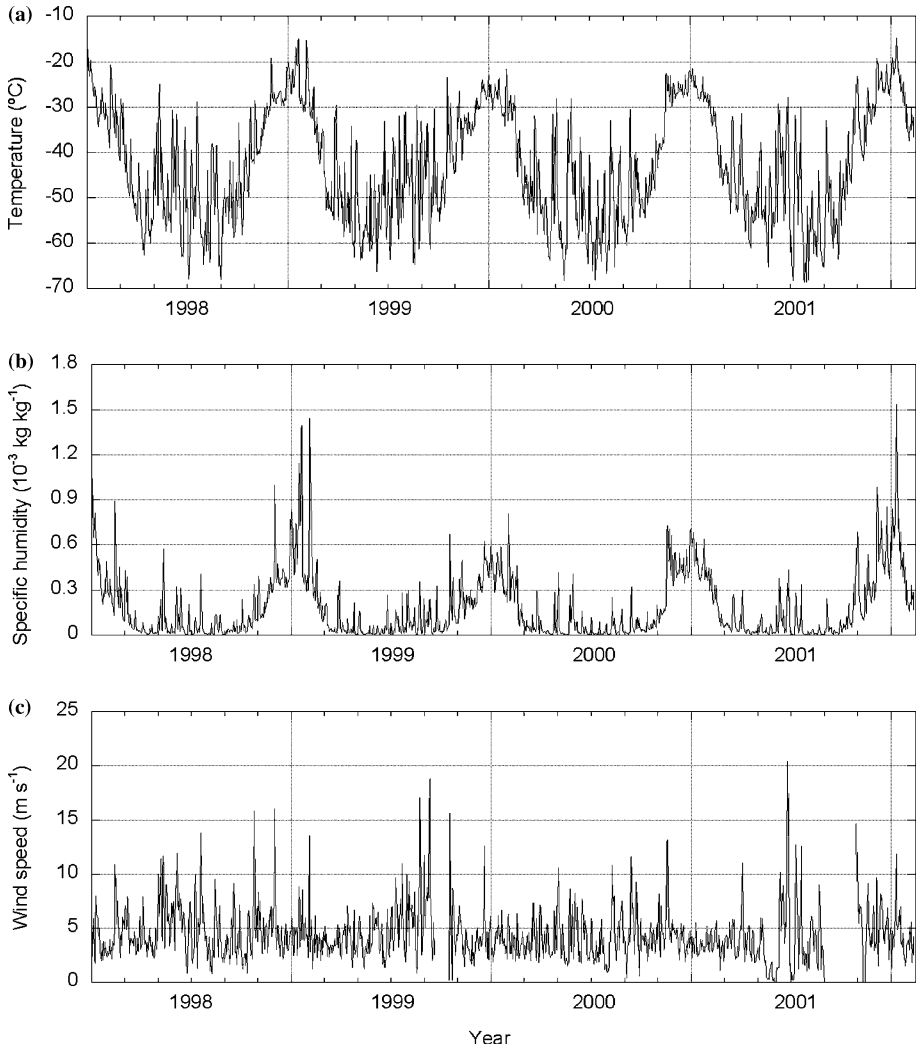

Figure 5. Daily mean AWS data of temperature (a), specific humidity (b) and wind speed (c) at 2-m height at Kohnen station over the 4-year period prior to and including the ENABLE period. Gaps in wind speed data occur when the sensor is fixed by icing.

and coreless winter. Specific humidity is strongly temperature dependent and therefore follows the temperature seasonal cycle (Figure 5b). In the wintertime specific humidity seldom exceeds 0.5×10^{-3} kg kg^{-1}, and only on warm summer days is 1.5×10^{-3} kg kg^{-1} reached. The lower panel shows no seasonal cycle in wind speed, and a daily mean wind speed of at least 2 m s^{-1} is nearly always present. Only a few times per year do synoptic perturbations penetrate the Antarctic plateau from the Weddell Sea (Noone et al., 1999), these events being characterised by relatively high T, q and u at AWS 9.

The period of measurement described herein lasted from 8 January until 9 February 2002. The mean 2-m temperature, specific humidity and wind speed during this period were −27.5 °C, 0.52×10^{-3} kg kg^{-1} and 4.1 m s^{-1} at Kohnen. Table III shows that the AWS data of the same period agree well with these measurements. Furthermore, the table shows that the mean general meteorological conditions were not extraordinary compared to the same period in the previous years (1998 to 2001). Temperature, specific humidity and wind speed for this period at 2-m height are presented in half-hourly and daily means in Figure 6. A strong daily cycle is present in all three parameters. At the beginning of the period conditions were relatively warm with daily temperatures between −25 and −14 °C and a maximum of approximately −12 °C. In this period daily mean 2-m wind speeds were high (5 to 11 m s^{-1}) and specific humidity was over 0.6×10^{-3} kg kg^{-1}. After this the atmospheric surface layer cooled, which is directly related to the increasing solar zenith angle. At the end of the period daily mean temperatures fell below −30 °C, the wind speed varied between approximately 1.5 m s^{-1} at night and 5 m s^{-1} during the day and specific humidity between 0.2 and 0.4×10^{-3} kg kg^{-1}. Although Figure 6 shows that, in general, 2-m wind speeds were stronger during the day than at night, this does not indicate the absence of katabatic forcing at night, because the 2-m wind speed is strongly influenced by the stability-related change in curvature of the wind speed profile. The full wind speed profile, as measured with a tethered balloon, did show a significant influence of katabatic forcing during clear nights.

The daily mean cloud cover during ENABLE as determined from observations is presented in Figure 7. The first 6 days of the experiment were overcast, caused by a low pressure system advecting warm and moist air from the south Atlantic ocean. During the rest of ENABLE thin ice clouds with a relatively low optical thickness were the most common clouds.

Concluding this section, the near-surface meteorological conditions during ENABLE compare well to the conditions measured by AWS 9 in the

TABLE III

Mean AWS data of 2-m temperature (°C), specific humidity (kg kg^{-1}), wind speed (m s^{-1}), net shortwave radiation and net longwave radiation (W m^{-2}) in the period 8 January to 9 February from 1998 to 2002.

	1998	1999	2000	2001	2002
T	−29.5	−24.3	−28.8	−27.5	−27.4
q	0.36×10^{-3}	0.65×10^{-3}	0.39×10^{-3}	0.42×10^{-3}	0.52×10^{-3}
U	3.5	4.8	4.0	3.4	4.5
S_N	62	57	62	61	54
L_N	−60	−51	−56	−55	−46

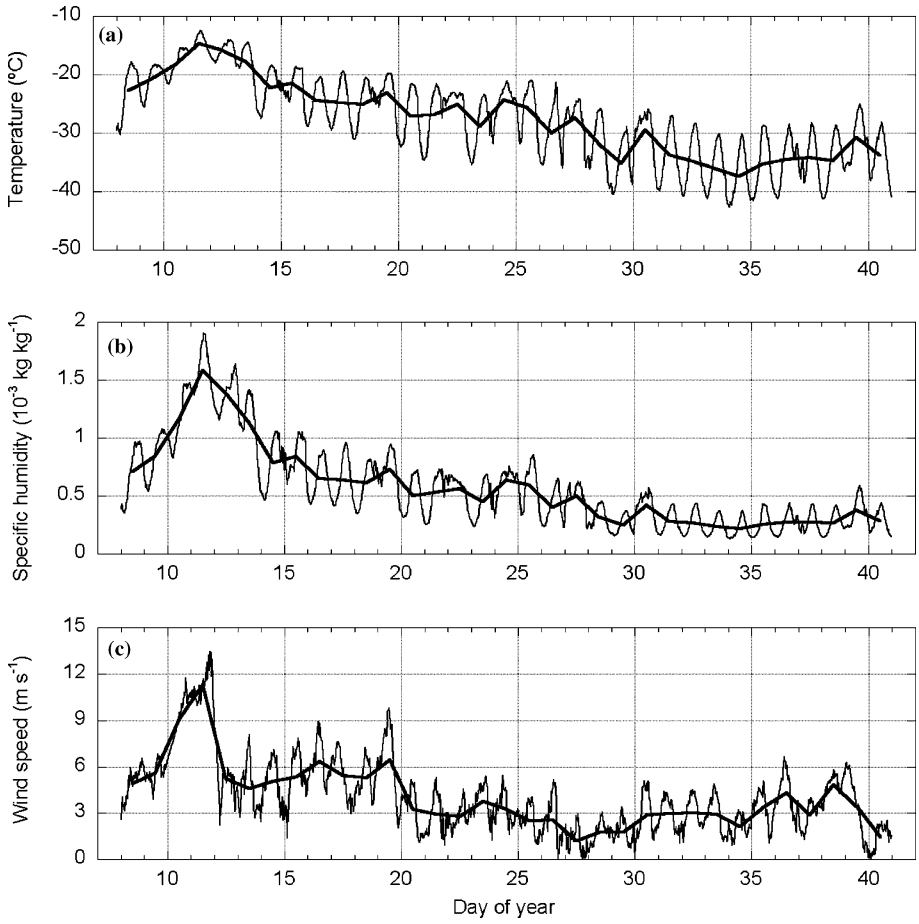

Figure 6. Half-hourly means (thin lines) and daily means (thick lines) of 2-m temperature (a), specific humidity (b) and wind speed (c) during ENABLE.

years prior to the experiment. Assuming that the observations of these 4 years give us a good estimate of the average conditions at Kohnen, this eliminates one possible cause of differences between this study and other studies.

4.2. Surface energy balance

4.2.1. *Radiative Fluxes*

Figure 8 shows daily means of the energy balance components during ENABLE. The daily mean S_N (Figure 8a) is high on days with low cloud cover (Figure 7) and high solar elevation with values of approximately

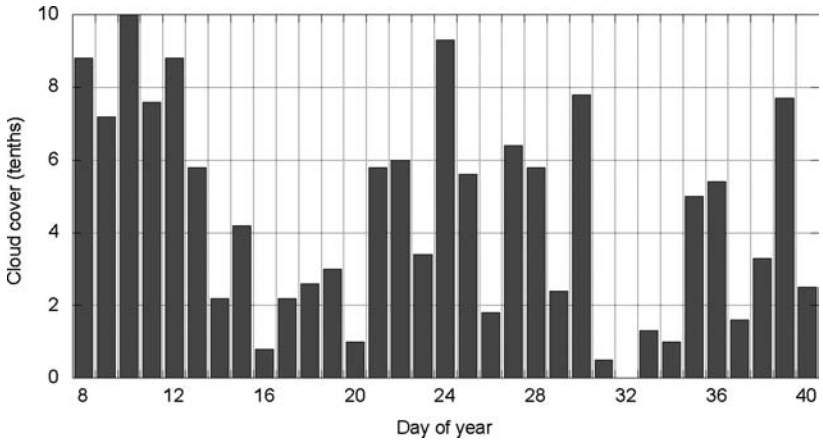

Figure 7. Daily mean cloud cover during ENABLE.

70 W m^{-2}. During overcast days, and towards the end of the experiment when solar elevation was low, daily mean S_N values were 25–35 W m^{-2}. Over the entire period net shortwave radiation has a mean value of 47 W m^{-2} (Table IV). The difference with mean S_N measured by AWS 9 (54 W m^{-2}, Table III) is significant; this is chiefly due to spatial differences in surface albedo or to inaccuracies introduced by AWS maintenance during the period of ENABLE.

Daily mean surface albedo is shown in Figure 9; the albedo during ENABLE ranged from 0.83 to 0.92, with a period mean value of 0.86. As explained in Section 2.2.1, the albedo depends on cloud amount and solar elevation. In agreement with these factors, the figure shows high albedo for overcast situations, obtaining its maximum value during the overcast period of days 10 to 12, and high albedo towards the end of the experiment when solar elevation was low. However, high amounts of snowdrift were observed during the strong-wind event of days 10 to 12 and snowfall is likely to have occurred in this period, both of which are possibly additional causes of high surface albedo.

Net shortwave radiation is balanced mostly by net longwave radiation. Net longwave radiation is often negative, as the emitted radiation by the snow surface cannot be balanced by the radiation emitted by the generally cold and dry atmosphere. Cloudy conditions are easily detected; the daily mean L_N on cloudy days has a low absolute value between 0 and −30 W m^{-2}, while during days with clear skies the surface loses between −50 and −75 W m^{-2} (Figure 8a). Net longwave radiation over the entire experiment was −48 W m^{-2} (Table IV), which agrees well with the mean L_N value measured by AWS 9 (−46 W m^{-2}).

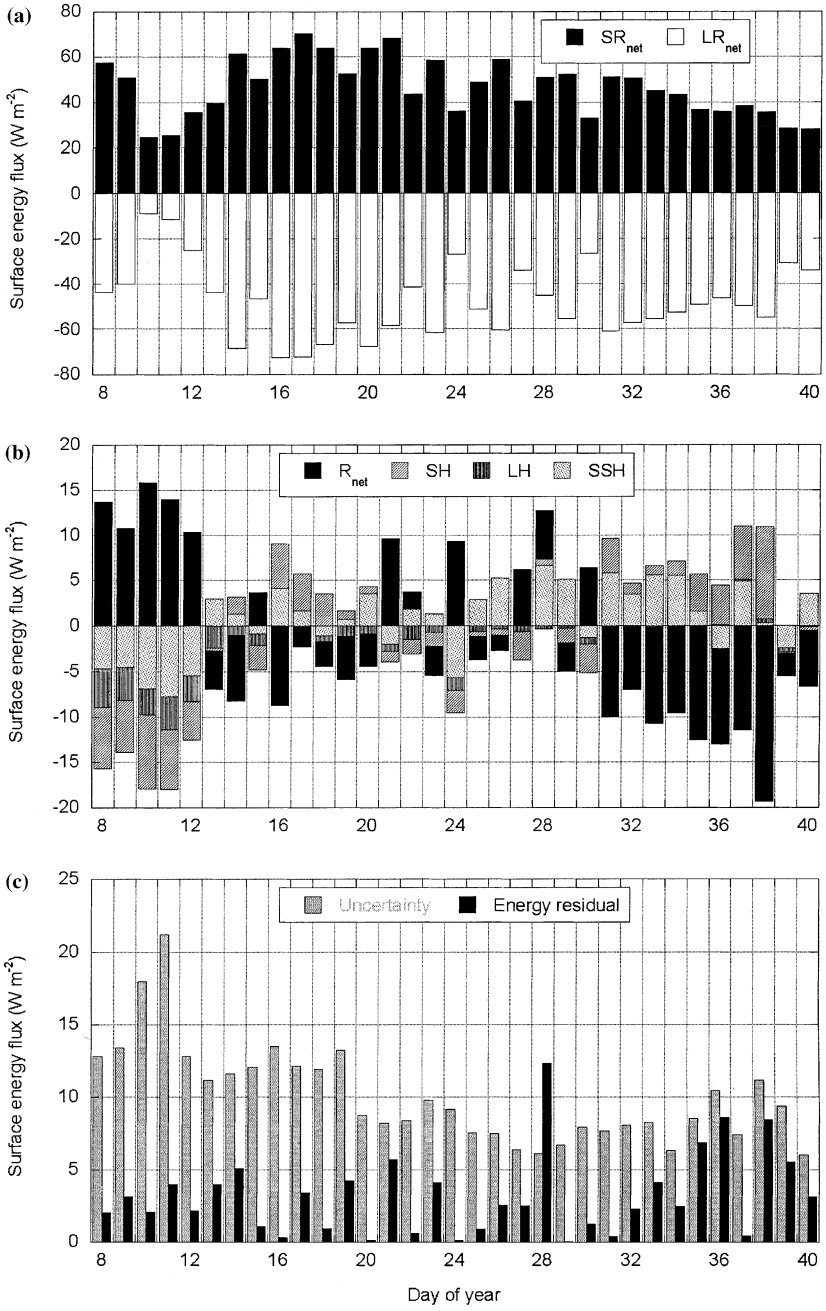

Figure 8. Daily means of net shortwave and longwave radiation (a) and net radiation, sensible heat, latent heat and sub-surface heat flux (b). Positive fluxes in a and b are directed towards the surface. Absolute value of daily mean residual energy of the SEB and the uncertainty related to error in measurement and theory are compared in (c).

TABLE IV
Mean values of energy balance components and standard deviations of daily means at Kohnen from 8 January to 9 February 2002. Values are in W m^{-2}.

	Mean	Standard deviation
$S\downarrow$	334.1	43.5
$S\uparrow$	−287.3	32.2
S_N	46.8	12.8
$L\downarrow$	157.6	33.7
$L\uparrow$	−205.5	23.7
L_N	−47.9	16.3
R_N	−1.1	8.9
H	−0.0	4.0
$\lambda_s E$	−1.0	1.2
G	0.7	4.0

Generally speaking, during days with clear-sky conditions the surface radiatively cools and during overcast days the snow surface warms (Figure 8b). So, despite the fact that clouds block shortwave radiation and increase surface albedo, the positive effect of clouds on net longwave radiation dominates the radiation balance (the radiation paradox; Ambach, 1974). Figure 8b also shows that daily mean net radiation (R_N) changed from positive to negative during ENABLE, which signifies the transition from summer to winter. Over the entire period, R_N was a small sink for surface heat (−1.1 W m^{-2}).

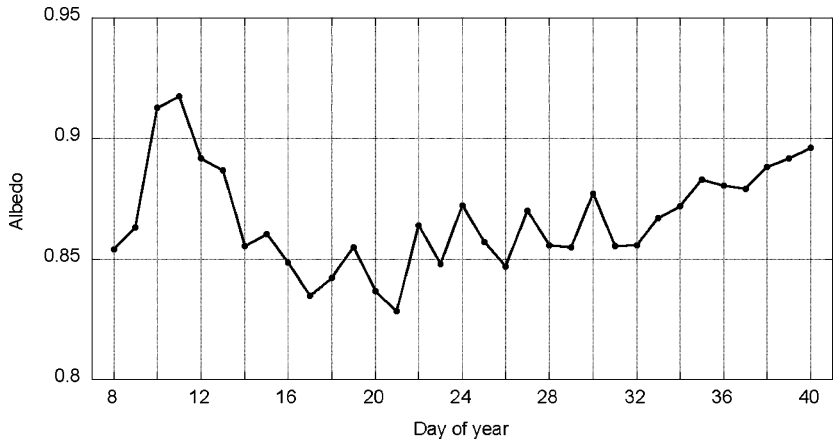

Figure 9. Daily mean albedo during ENABLE.

4.2.2. *Turbulent Heat Fluxes*

Figure 8b shows that during ENABLE the daily mean turbulent heat fluxes and net radiation tend to be of opposite sign. Early in the period this resulted in daily mean H values of -4 to -8 W m^{-2} and $\lambda_s E$ values of -2 to -4 W m^{-2}. Further towards the end of the experiment, when strong radiative cooling of the surface occurred due to low solar elevation and low cloud amount, the daily mean H was positive with values between 1 and 10 W m^{-2}. The low temperatures did not allow for large vertical gradients in specific humidity, causing low daily mean $\lambda_s E$ values between -0.1 and 0.4 W m^{-2}. The shift from negative to positive turbulent heat flux values results in near-zero values averaged over the entire period (Table IV).

Available eddy-correlation measurements of the sensible heat flux were used to validate the bulk flux calculations (Figure 10a). With a correlation coefficient of 0.95 and a RMSD of 3.0 W m^{-2} the calculations are in good agreement with the direct measurements. A mean difference of -0.9 W m^{-2} suggests a slight underestimation of calculated bulk fluxes of sensible heat.

Since eddy-correlation measurements of latent heat were unsuccessful, but a check of the performance of the calculations is desirable, the latent heat flux is estimated from the sonic anemometer data using the modified Bowen ratio method (Liu and Foken, 2001). For a known Bowen ratio ($B = H\ (\lambda_s E)^{-1}$) latent heat can be determined from the eddy-correlation (subscript 'ec') measurements of sensible heat:

$$H_{L,ec} = \frac{H_{S,ec}}{B} \approx H_{S,ec} \frac{L_s}{c_p} \frac{\Delta \overline{q}}{\Delta \overline{T}}. \tag{14}$$

Here, first order K-theory approximation is applied, which relates the gradient of a parameter (a) to the covariance of that parameter and the vertical component of wind speed fluctuations: $\overline{w'a'} = -K_a \frac{\Delta \overline{a}}{\Delta z}$. Because K is assumed equal for moisture and heat it is eliminated from Equation (14). The specific humidity and temperature differences $\Delta \overline{q}$ and $\Delta \overline{T}$ are determined between the surface and 2-m height. The latent heat flux thus obtained is compared to the 'calculated' latent heat flux in Figure 10b. The agreement is reasonable with a correlation coefficient of 0.47 and a RMSD of 1.6 W m^{-2}, although the calculated values are systematically lower than the measured values (mean difference $= -0.7$ W m^{-2}). The scatter in Figure 10b is larger than in Figure 10a since, among other reasons, the modified Bowen ratio method is sensitive to situations when vertical temperature gradients are small.

4.2.3. *Sub-Surface Heat Flux*

During ENABLE, the mean sub-surface heat flux was slightly positive (0.7 W m^{-2}, Table IV). Like the turbulent heat fluxes, the sub-surface heat flux generally opposes the mean radiative flux. From the daily means in Figure 8, we can conclude that G is comparable to H in magnitude, and in a

similar fashion G is negative during the first few days and becomes positive at the end of the period. Daily mean G values ranged from -8 to $+7$ W m^{-2}. Figure 11 compares measured and calculated snow temperatures at 0.2-m and 0.4-m depths to check the accuracy of the calculations. In spite of the approximations made, the calculated and measured snow temperatures agree

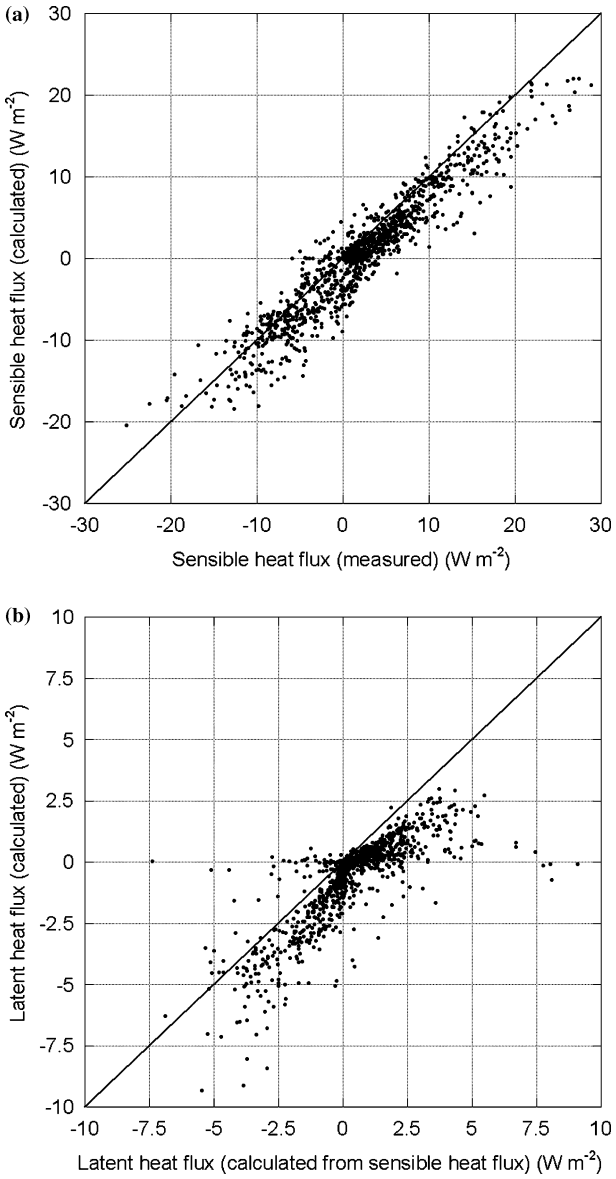

Figure 10. Comparison of calculated and measured half-hourly values of the sensible (a) and latent (b) heat flux.

well. The differences in temperature can easily be explained by snow density variations, for example. Note that the density profile in Figure 4 represents the average profile for the surroundings of Kohnen, not one specific location. Therefore G presented in Figure 8b can be interpreted as the mean G for a larger area.

4.3. Sensitivity analysis

The sensitivity of the calculated mean energy balance components to small variations in input parameters is presented in Table V. The displayed parameters are changed uniformly over the entire period and one at a time.

Increasing the temperature by 1 °C at the surface (equivalent to a change in $L\uparrow$ by 3.3 W m^{-2}) or at 2-m height has an opposite effect on the sensible heat flux. In the latter case there is an increased vertical temperature gradient, resulting in an increase in mean sensible heat of 4.4 W m^{-2}. A rise in surface temperature facilitates convection and decreases the sensible heat by 4.7 W m^{-2} and latent heat by 1.1 W m^{-2}. The sub-surface heat flux then decreases by 0.3 W m^{-2}. When the specific humidity of the air is increased by 0.05×10^{-3} kg kg^{-1}, more moisture is available for transport to the surface, increasing the latent heat flux by 0.7 W m^{-2}.

A positive change of 0.5 m s^{-1} in wind speed increases u_* and thus the absolute size of the turbulent heat fluxes (Equations (5) and (6)). The increase

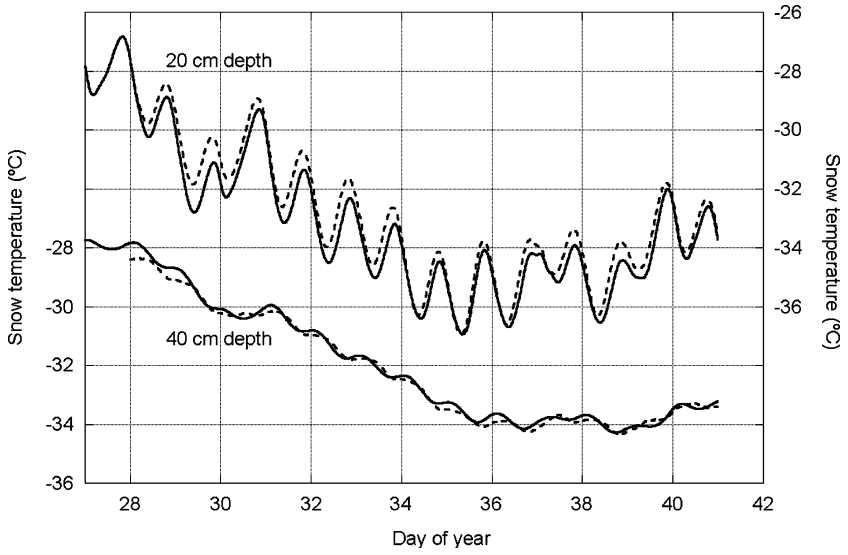

Figure 11. Measured (dashed line) and calculated snow temperatures (solid line) at 0.2 and 0.4 m.

in u_* is noticed most at low wind speeds (high stability). Since these low wind speeds occurred at the end of the measuring period when the daily mean sensible heat fluxes were positive (Figure 8b), the period mean sensible heat flux increases, though by just 0.5 W m^{-2}. Due to the very small latent heat fluxes at the end of the period an increase in wind speed chiefly increases the size of $\lambda_s E$ at the beginning of the period, which becomes slightly more negative over the entire period by −0.1 W m^{-2}.

Equations (7), (8) and (9) show that turbulent fluxes could be sensitive to changes in $z_{0,T,q}$, especially when these roughness lengths are small. Table V shows that this sensitivity is small; if z_0 is increased by a factor of five, mean sensible and latent heat fluxes increase in absolute size by only 0.2 and 0.1 W m^{-2}, respectively. When surface roughness is lowered by a factor of five, the fluxes become smaller by similar amounts. Changes are generally small, since a different roughness length mainly influences the amplitude of the daily cycle and not the daily means. The same occurs when the stability correction is not taken into account or changes in snow density or its thermal conductivity are imposed; the period mean values of the sub-surface heat flux display a small change. This shows that the magnitude of the SEB terms obtained is robust. A detailed discussion of the daily cycle of the energy balance is presented by Van As et al. (2005).

5. Discussion and Conclusions

We presented the SEB of the high Antarctic plateau during summer. Equation (1) states that for a skin surface layer without heat capacity or given

TABLE V

Change in the surface energy balance components over the measuring period with respect to the reference case as a results of varying input parameters. Values are in W m^{-2}.

	H	$\lambda_s E$	G
$T(0)$ + 1 °C	−4.7	−1.1	−0.3
T (2 m) + 1 °C	+4.4	+0.0	0
q (2 m) + 0.05×10^{-3} kg kg^{-1}	+0.0	+0.7	0
u (2 m) + 0.5 m s^{-1}	+0.5	−0.1	0
$z_0 \times 5$	+0.1	−0.2	0
$z_0/5$	−0.0	+0.2	0
$\psi_{m,h,q} = 0$	+1.5	+0.1	0
ρ_{snow} + 50 kg m^{-3}	0	0	+0.1
k_e + 0.1 W m^{-1} K^{-1}	0	0	−0.1

temperature all surface energy components are balanced. Figure 8c shows that the various measured and calculated components do not always balance exactly; on most days the daily mean residual energy of the SEB is 0–5 W m^{-2}. The main source of uncertainty is net radiation. The difficulty is that the Antarctic summer radiation balance consists of several large terms of approximately the same size, which results in a small R_N with a relatively large uncertainty of measurement. To illustrate the uncertainty in the SEB that originates from sensor accuracy, this has been plotted with the daily mean energy residual in Figure 8c. Clearly, the imbalance during all days in Figure 8b can be explained by measurement uncertainty, with the exception of day 28. In the morning of this day icing affected multiple sensors ($S\downarrow$, $L\downarrow$, $L\uparrow$, T, q and possibly u). We also notice in Figure 8c that, while accuracy increases towards the end of the period due to the decreasing sizes of surface energy fluxes, the residual term of the SEB increases. This might be related to decreasing sensor accuracy at low temperatures and large solar zenith angles.

As an alternative SEB calculation method, we can choose not to constrain $T(0)$ by observations, but to find the value of T(0) for which all surface energy fluxes are in balance. Figure 12 compares these surface temperatures to the measured radiative surface temperatures. As can be seen, agreement is good, with a root mean square difference of 1.1 °C, which is equivalent to a difference of 3.7 W m^{-2} in longwave radiation, which is accurate for SEB calculations. This gives confidence in the calculated SEB. Again, the largest errors occur in the morning of 28 January 2002 (circles). For temperatures below –40 °C a small systematic difference is found between the calculated and the measured temperatures.

The sub-surface heat flux calculations produced snow temperatures that also agreed well with the measurements, in spite of the assumptions made. For instance, ventilation of the near-surface snow was not included, the density profile we used is only an approximation of an otherwise irregularly stratified layer of snow (Figure 4) and the passing of snow dunes caused the snow temperature measurements to be taken at variable depth. Apparently these factors have a relatively small impact on the sub-surface heat transport.

To put the ENABLE observations into a temporal perspective, Figure 13 shows the annual cycle of the energy balance components at AWS 9 (based on monthly means, averaged for 1998–2001). The AWS energy balance has been computed using data treatment techniques similar to the ones presented in this paper; a difference is that at the AWS the energy balance closure assumption (mentioned above) was made to obtain $T(0)$, mainly to avoid problems associated with icing of the radiation sensor during winter. Except for the wind speed sensor, the AWS is equipped with identical sensors as used for this SEB study, which facilitates comparison. However, the AWS sensors measure at a much lower frequency, and are not

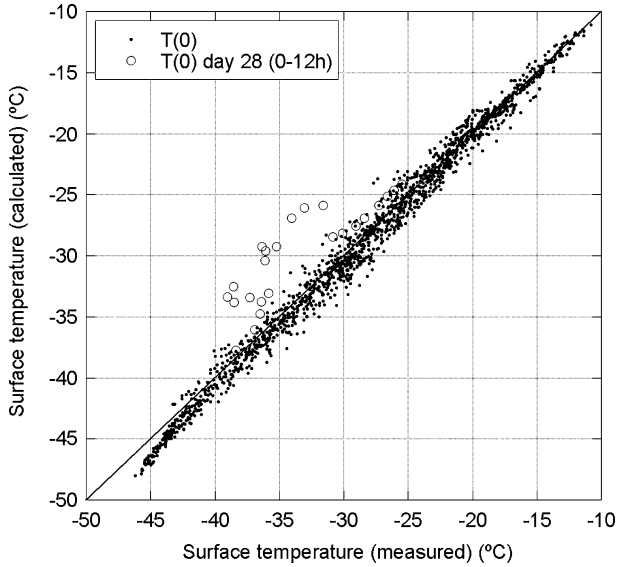

Figure 12. Half-hourly surface temperatures for which SEB = 0 plotted against the observed surface temperature during ENABLE. Temperatures between 0000 h and 1200 h on 28 January 2002 are marked with circles.

ventilated, nor checked for tilt or icing regularly. Furthermore, no eddy-correlation measurements are performed at the AWS to verify the calculated bulk fluxes of sensible and latent heat. Though less accurate, the AWS readings give us a clear idea of temporal SEB variability on monthly time scales near Kohnen base.

The period of ENABLE (grey area in Figure 13) fell after the high summer period recognized as the peak in absorbed shortwave radiation in December. Instead, conditions during ENABLE were representative of the transition from summer to winter and coincide with the steepest gradients in all energy balance components: from mid-January to mid-February, the net radiation changes from positive to negative and the sensible heat flux from negative to positive, as does the sub-surface heat flux. The latent heat flux becomes small in response to low ambient temperatures. The change in regime from net heating to net cooling of the snow pack and atmosphere is also clearly visible in the ENABLE daily mean fluxes (Figure 8b), with all components behaving as described above. As a result of averaging over this regime change, average values of net radiation and sensible heat flux/sub surface heat flux are small (Table IV).

This strong dependency of the average fluxes on the exact timing of the experiment and the short duration of most experiments in Antarctica makes it difficult to compare results among experiments. Table VI makes an attempt and lists average fluxes for several summertime meteorological

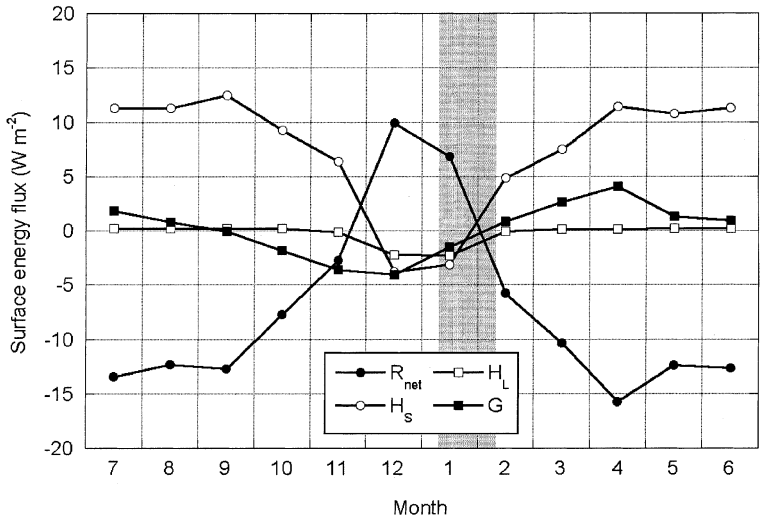

Figure 13. Monthly mean net radiation, sensible heat, latent heat and sub-surface heat flux, determined from four years of AWS 9 data. The grey area indicates the period of ENABLE.

experiments in Antarctica at high elevations. As can be seen, there is a large spread in reported fluxes for net radiation and turbulent heat fluxes, even for experiments at the same location (South Pole). Longwave radiative loss at Kohnen is smaller than at site 7 of Bintanja, mainly because of a larger H there. The sites with positive R_N (Vostok, Mizuho and Pionerskaya) are characterized by lower albedo ($\alpha \leq 0.83$), resulting in higher surface temperature and greater convection. At the last two sites the low albedo is presumably caused by strong metamorphosis due to katabatic winds. Also note that some of these studies calculated the latent heat flux as a residual of the energy balance, leading to a clear overestimate as in Dalrymple et al. (1966).

Acknowledgements

We thank Wim Boot, Henk Snellen, Piet Jonker, Michiel Helsen, Arjen van Dijk, Richard Bintanja, Lisette Klok and Alec van Herwijnen. Furthermore, we thank the Alfred Wegener Institute (AWI) for providing the logistics and the Netherlands Organisation for Scientific Research (NWO) for the financial support for the expedition. This work is a contribution to the 'European Project for Ice Coring in Antarctica' (EPICA), a joint ESF (European Science Foundation)/EC scientific programme, funded by the European Commission and by national contributions from Belgium, Denmark, France, Germany, Italy, the Netherlands, Norway, Sweden, Switzerland and the United Kingdom. This is EPICA publication no. 117.

TABLE VI

Observed mean summer energy balance components (in Wm^{-2}) in Antarctica with elevation (in m) larger than 2000 m. Values are in W m^{-2}. D = December, J = January, F = February and M = March.

Location	Elevation	Months	α	S_N	L_N	R_N	H	$\lambda_s E$	$H+\lambda_s E$
Vostok[a]	3488	J	0.83	+68	−48	+20			
Kohnen[b]	2892	JF	0.86	+47	−48	−1	0	−1	−1
South Pole[c]	2835	F	0.85			−19	+9	+9	+18
South Pole[d]	2835	DJFM	0.84			−20			+24
Pionerskaya[e]	2740	J	0.82			+24	−3	+1	−2
Mizuho[f]	2230	D	0.77			+20	−7	−8	−15
Site 7[g]	2100	J	0.86	+50	−64	−14	+20	−6	+14

[a] King and Turner (1997).
[b] This study.
[c] Dalrymple et al. (1966).
[d] Carroll (1982).
[e] Schlatter (1972).
[f] Ohata et al. (1985).
[g] Bintanja (2000).

References

Allison, I., Wendler, G., and Radok, U.: 1993, 'Climatology of the East Antarctic Ice-Sheet (100-degrees-E to 140-degrees-E) Derived from Automatic Weather Stations', *J. Geophys. Res.* **98**(D5), 8815–8823.

Ambach, W.: 1974, 'The Influence of Cloudiness on the Net Radiation Balance of a Snow Surface with High Albedo', *J. Glaciol.* **13**, 73–84.

Anderson, P. S.: 1994, 'A Method for Rescaling Humidity Sensors at Temperatures Well Below Freezing', *J. Atmos. Oceanic Tech.* **11**, 1388–1391.

Andreas, E. L.: 1987, 'A Theory for the Scalar Roughness and the Scalar Transfer Coefficients over Snow and Sea Ice', *Boundary-Layer Meteorol.* **38**, 159–184.

Andreas, E. L.: 2002, 'Parameterizing Scalar Transfer over Snow and Ice: A Review', *J. Hydrometeorol.* **3**, 417–432.

Bintanja, R.: 2000, 'Surface Heat Budget of Antarctic Snow and Blue Ice: Interpretation of Spatial and Temporal Variability', *J. Geophys. Res.* **105**, 24387–24407.

Bintanja, R. and Van den Broeke, M. R.: 1995, 'The Surface Energy Balance of Antarctic Snow and Blue Ice', *J. Appl. Meteorol.* **34**, 902–926.

Box, J. E. and Steffen, K.: 2001, 'Sublimation on the Greenland Ice Sheet from Automated Weather Station Observations', *J. Geophys. Res.* **106**(D24), 33965–33981.

Brandt, R. E. and Warren, S. G.: 1993, 'Solar-Heating Rates and Temperature Profiles in Antarctic Snow and Ice', *J. Glaciol.* **39**(131), 99–110.

Carroll, J. J.: 1982, 'Long-Term Means and Short-Term Variability of the Surface Energy Balance Components at the South Pole', *J. Geophys. Res.* **87**, 4277–4286.

Curry, J. A. and Webster, P. J.: 1999, *Thermodynamics of Atmospheres and Oceans*, Academic Press, London, 467 pp.

Dalrymple, P. C., Lettau, H. H., and Wollaston, S. H.: 1966, 'South Pole Micrometeorological Program: Data Analysis, in Studies in Antarctic Meteorology', in M. J. Rubin (ed.), *Antarctic Research Series*, Vol. 9, AGU, Washington DC, pp. 13–57.

Dyer, A. J.: 1974, 'A Review of Flux-Profile Relationships', *Boundary-Layer Meteorol.* **7**, 363–372.

Fortuin, J. P. F. and Oerlemans, J.: 1992, 'An Atmospheric Model for Simulating the Mass Balance and Temperature on the Antarctic Ice Sheet', *Z. Gletscherkd. Glazialgeol.* **26**, 31–z56.

Genthon, C. and Braun, A.: 1995, 'ECMWF Analyses and Predictions of the Surface Climate of Greenland and Antarctica', *J. Climate* **8**, 2324–2332.

Holtslag, A. A. M. and De Bruin, H. A. R.: 1988, 'Applied Modelling of the Night-Time Surface Energy Balance over Land', *J. Appl. Meteorol.* **27**, 689–704.

Jonsson, S.: 1995, 'Synoptic Forcing of Wind and Temperature in a Large Cirque 300 km from the Coast of East Antarctica', *Antarct. Sci.* **7**, 409–420.

King, J. C. and Anderson, P. S.: 1994, 'Heat and Water-Vapor Fluxes and Scalar Roughness Lengths over an Antarctic Ice Shelf', *Boundary-Layer Meteorol.* **69**, 101–121.

King, J. C. and Connolley, W. M.: 1997, 'Validation of the Surface Energy Balance over the Antarctic Ice Sheets in the U.K. Meteorological Office Unified Climate Model', *J. Climate* **10**, 1273–1287.

King, J. C. and Turner, J.: 1997, *Antarctic Meteorology and Climatology*, Cambridge University Press, Cambridge, 409 pp.

King, J. C., Anderson, P. S., Smith, M. C., and Mobbs, S. D.: 1996, 'The Surface Energy and Mass Balance at Halley, Antarctica during Winter', *J. Geophys. Res.* **101**(D14), 19119–19128.

König-Langlo, G., King, J. C., and Pettré, P.: 1998, 'Climatology of the Coastal Antarctic Stations Dumont d'Urville, Neumayer, and Halley', *J. Geophys. Res.* **103**(D9), 10935–10946.

Liu, H. and Foken, T.: 2001, 'A Modified Bowen Ratio Method to Determine Sensible and Latent Heat Fluxes', *Meteorol. Z.* **10**, 71–80.

Liu, H., Jezek, K., Li, B., and Zhao, Z.: 2001, 'Radarsat Antarctic Mapping Project Digital Elevation Model Version 2. National Snow and Ice Data Center, Boulder, CO: Digital media.

Noone, D., Turner, J., and Mulvaney, R.: 1999, 'Atmospheric Signals and Characteristics of Accumulation in Dronning Maud Land, Antarctica', *J. Geophys. Res.* **104**(D16), 19191–19211.

Ohata, T., Ishikawa, N., Kobayashi, S., and Kawaguchi, S.: 1985, 'Heat Balance at the Snow Surface in a Katabatic Wind Zone, East Antarctica', *Ann. Glaciol.* **6**, 174–177.

Östin, R. and Andersson, S.: 1991, 'Frost Growth Parameters in a Forced Air Stream', *Int. J. Heat Mass Transfer* **34**, 1009–1017.

Paulson, C. A.: 1970, 'The Mathematical Representation of Wind Speed and Temperature Profiles in the Unstable Atmospheric Surface Layer', *J. Appl. Meteorol.* **9**, 857–861.

Reijmer, C. H.: 2001, *Antarctic Meteorology: A Study with Automatic Weather Stations*, Ph.D. Dissertation, Utrecht University, Utrecht, 158 pp.

Reijmer, C. H. and Oerlemans, J.: 2002, 'Temporal and Spatial Variability of the Surface Energy Balance in Dronning Maud Land, East Antarctica', *J. Geophys. Res.* **107**(D24), 4759–4770.

Reijmer, C. H., Greuell, W., and Oerlemans, J.: 1999, 'The Annual Cycle of Meteorological Variables and the Surface Energy Balance on Berkner Island, Antarctica', *Ann. Glaciol.* **29**, 49–54.

Schlatter, T. W.: 1972, 'The Local Surface Energy Balance and Subsurface Temperature Regime in Antarctica', *J. Appl. Meteorol.* **11**, 1048–1062.

Schotanus, P., Nieuwstadt, F. T. M., and De Bruin, H. A. R.: 1983, 'Temperature Measurement with a Sonic Anemometer and its Application to Heat and Moisture Fluxes', *Boundary-Layer Meteorol.* **26**, 81–93.

Stearns, C. R. and Weidner, G. A.: 1993, 'Sensible and Latent Heat Flux Estimates in Antarctica', in D. H. Bromwich and C. R. Stearns (eds.), *Antarctic Meteorology and Climatology, Studies Based on Automatic Weather Stations, Antarctic Research Series*, Vol. 61, AGU, Washington DC, pp. 109–138.

Van As, D., Van den Broeke, M. R., and Van de Wal, R. S. W.: 2005, 'Daily Cycle of Surface Layer and Energy Balance on the High Antarctic Plateau', *Antarct. Sci.*, in press.

Van den Broeke, M. R., Reijmer, C. H., and Van de Wal, R. S. W.: 2004a, 'A Study of the Surface Mass Balance in Dronning Maud Land, Antarctica, Using Automatic Weather Stations', *J. Glaciol.*, in press.

Van den Broeke, M. R., Van As, D., Reijmer, C. H., and Van de Wal, R. S. W.: 2004b, 'Assessing and Improving the Quality of Unattended Radiation Observations in Antarctica', *J. Atmos. Oceanic Tech.* **21**, 1417–1431.

Van den Broeke, M. R., Van de Wal, R. S. W., and Wild, M.: 1997, 'Representation of Antarctic Katabatic Winds in a High Resolution GCM and a Note on their Climate Sensitivity', *J. Climate* **10**, 3111–3130.

Van Lipzig, N. P. M., Van Meijgaard, E., and Oerlemans, J.: 1999, 'Evaluation of a Regional Atmospheric Model Using Measurements of Surface Heat Exchange Processes from a Site in Antarctica', *Mon. Wea. Rev.* **127**, 1994–2011.

Weller, G.: 1980, 'Spatial and Temporal Variations in the South Polar Surface Energy Balance', *Mon. Wea. Rev.* **108**, 2006–2014.

Wendler, G., Ishikawa, N., and Kodama, Y.: 1988, 'The Heat-Balance of the Icy Slope of Adelie-Land, Eastern Antarctica', *J. Appl. Meteorol.* **27**, 52–65.

Wilczak, J. M., Oncley, S. P., and Stage, S. A.: 2001, 'Sonic Anemometer Tilt Correction Algorithms', *Boundary-Layer Meteorol.* **99**, 127–150.

Wiscombe, W. J. and Warren, S. G.: 1980, 'A Model for the Spectral Albedo of Snow. I: Pure Snow', *J. Atmos. Sci.* **37**, 2712–2733.